

1 **Effects of radiative cooling on advection fog over the Northwest**

2 **Pacific Ocean: Observations and large eddy simulations**

3 Liu Yang¹, Saisai Ding², Jing-Wu Liu^{2*}, Su-Ping Zhang²

4 ¹College of Aviation Meteorology, Civil Aviation Flight University of China,

5 Guanghan, China

6 ² Frontier Science Center for Deep Ocean Multispheres and Earth System

7 (FDOMES), Physical Oceanography Laboratory, and Ocean–Atmosphere Interaction

8 and Climate Laboratory, Ocean University of China, Qingdao, China

9

* Corresponding author: Jing-Wu Liu, Ocean University of China, 238 Songling Road, Qingdao, 266100, P. R. China

Email: liujingwu@126.com; liujingwu@ouc.edu.cn

Abstract

10
11 During boreal summer, prevailing southerlies traverse the sharp sea surface
12 temperature (SST) front in the Northwest Pacific (NWP) Ocean, creating a stable air-
13 sea interface characterized by surface air temperature (SAT) higher than SST, which
14 promotes the frequent occurrence of advection fog. However, long-term shipborne
15 observations reveal that during episodes of advection fog, SAT usually decreases below
16 SST, with a peak relative frequency (~34.5%) to all fog observations before sunrise and
17 a minimum relative frequency (~18.8%) before sunset. From a Lagrangian perspective,
18 this study employs a turbulence-closure large-eddy simulation (LES) model to trace a
19 fog column across the SST front and investigates how SAT drops below SST during an
20 advection fog event. The LES model, incorporating constant solar radiation,
21 successfully simulates the evolution of advection fog and the negative **difference**
22 **between SAT and SST**. Simulation results show that once the near-surface air condenses,
23 thermal turbulence is generated by strong longwave radiation cooling (LWC) at the fog
24 top. The influence of LWC on the fog layer surpasses the cooling effect of the near-
25 surface mechanical turbulence ~2 hours after the fog formation, while the fog column
26 is still positioned over the SST front. When the fog column arrives **at** the cold flank of
27 the SST front, the top-down developing mixed layer induced by the LWC reaches the
28 surface, causing SAT to drop below SST. The LES model with diurnal solar radiation
29 **successfully simulates the observational** diurnal variation in SAT-SST during the fog
30 event, suggesting that the model captures the essential processes responsible for
31 negative SAT-SST. This study highlights the significance of fog-top cooling and its
32 associated thermal turbulence in the evolution of advection fog. Given the challenges
33 faced by numerical weather prediction models in forecasting sea fog, our findings
34 suggest that observations of negative SAT-SST during advection fog episodes present
35 an opportunity to enhance the performance of these models in simulating the thermal
36 turbulence induced by the LWC at the fog top.

37

38 1. Introduction

39 The northwest Pacific Ocean experiences heavy sea fog during summer (Wang,
40 1985; Koračin and Dorman, 2017), which is of great importance due to its significant
41 impact on maritime activities (Gultepe et al., 2007; Trémant, 1987). However, present
42 numerical weather prediction models struggle to accurately forecast sea fog (Gao et al.,
43 2007), partly because their coarse resolutions inadequately resolve boundary-layer
44 processes within the thin fog layer with depths of hundreds of meters (Yang et al., 2019).
45 Therefore, enhancing our understanding of turbulent boundary-layer processes
46 becomes imperative for refining the accuracy of sea fog predictions.

47 The sea surface temperature (SST) gradient associated with Kuroshio Extension
48 often triggers advection fog during summertime warm advection (Wang, 1985; Koračin
49 and Dorman, 2017). **Prevailing southerlies on the western flank of the subtropical high**
50 **transport warm, humid air across Kuroshio Extension front (Zhang et al., 2014; Long**
51 **et al., 2016; Koracin and Dorman, 2017), which cools the near-surface humid air**
52 **through mechanical turbulence, leading to air saturation and fog formation** (Taylor,
53 1917; Rodhe, 1962; Lewis et al., 2004; Gao et al., 2007; Yang et al., 2020). Nevertheless,
54 near-surface cooling induced by mechanical turbulence appears to be crucial in the
55 initial phase of advection fog (Hu et al., 2006).

56 Once fog forms, longwave radiation cooling (LWC) effect at the fog top
57 commences to influence fog evolution. Earlier observational studies conjectured that
58 the LWC at the fog top plays an important role in the fog's development and
59 maintenance (Douglas, 1930; Lamb, 1943; Petterssen, 1938; Findlater et al., 1989).
60 LWC at the fog top induces negative buoyancy and thermal turbulence (Bretherton and
61 Wyant, 1997; Gerber et al., 2005, 2013; Guan et al., 1997; Yamaguchi and Randall,
62 2008; Koračin and Dorman, 2017). This thermal turbulence further promotes vertical
63 mixing and cools the fog layer (Rogers and Koračin, 1992; Koracin et al., 2001, 2005;
64 Yang et al., 2018). Huang et al. (2015) identified a so-called thermal turbulence
65 interface, which separates thermal turbulence induced by the fog-top LWC and near-
66 surface mechanical turbulence. Despite previous studies recognizing the significance

67 of LWC at the fog top, its relative importance to near-surface cooling by mechanical
68 turbulence remains to be determined.

69 Observational evidence underscores the significance of LWC at fog top, as surface
70 air temperature (SAT) occasionally falls below SST during advection fog episodes. This
71 means that the sea surface acts to heat the fog layer (referred to as sea fog with sea
72 surface heating [ssH] hereafter). Instances of ssH fog have been reported in advection
73 fog events over the Yellow Sea (Zhang et al., 2012; Zhang and Ren, 2010), during the
74 haar peak over the North Sea (Lamb et al., 1943), and in the fog off the California coast
75 (Leipper, 1948, 1994), as well as off the northeastern coast of Scotland (Findlater et al.
76 1989). Based on long-term buoy observations, Yang et al. (2018) found that the relative
77 frequency of ssH fog to advection fog reaches up to ~30% over the Yellow Sea in
78 summer. Their composite analysis revealed that ssH fog is associated with stronger
79 atmospheric subsidence, a drier free atmosphere, and sharper capping inversions,
80 indicative of a crucial role of the fog-top LWC for ssH fog. However, limited
81 observations of the boundary-layer vertical structure over the sea inhibit the
82 understanding of how fog-top LWC influences advection fog and leads to a negative
83 SAT-SST.

84 In comparison to numerical weather prediction models, large eddy simulations
85 (LES) with higher resolutions are capable of explicitly resolving larger thermal
86 turbulent eddies within the boundary layer. LES has been successfully employed in
87 studies related to clouds (Bretherton and Wyant, 1997; Wyant et al., 1997; Stevens 2000,
88 2007; Savic-Jovci and Stevens, 2008; McGibbon and Bretherton, 2017) and continental
89 fog (Nakanishi, 2000; Bergot, 2013, 2016; Mazoyer et al. 2016; Maronga and Bosveld
90 2017; Schwenkel and Maronga 2019). Recently, the application of LES has extended
91 to sea fog (Yang et al., 2021; Wainwright and Richter, 2021). Yang et al. (2021) used
92 the climatological subsidence to force a LES model to study an advection fog event
93 over the NWP. They found that the fog-top thermal turbulence induced by the LWC
94 entrains the drier free atmospheric air into the boundary layer, which evaporates near-
95 surface fog droplets, leading to a transition of fog into stratus. This simulated fog-to-
96 stratus transition based on LES is consistent with that in long-term observations.

97 Wainwright and Richter (2021) attempted to use LES to examine the sensitivity of sea
98 fog to the cloud-droplet number concentration, turbulent mixing, and SAT-SST.

99 The present study primarily focuses on the ssH fog during advection fog episodes.
100 We first analyze the statistical features of the ssH fog over the NWP using long-term
101 shipborne observations. ssH fog was observed during the advection fog episode studied
102 by Yang et al. (2021). Thus, this study extends the LES simulation conducted by Yang
103 et al. (2021) by forcing the LES with more realistic free-atmospheric subsidence to
104 specifically investigate the boundary-layer processes responsible for ssH fog. We
105 quantify the heat budgets of the fog layer based on the LES results to compare the
106 effects of fog-top LWC and near-surface cooling and identify the interface between
107 thermal and mechanical turbulence. The results highlight the importance of the fog-top
108 cooling and its induced thermal turbulence on the evolution of advection fog.

109 The paper is organized as follows. Section 2 describes the data sets and methods
110 used in this study. Section 3 analyzes the observational characteristics of sea fog with
111 ssH over the NWP. Section 4 presents the simulation results obtained using constant
112 solar radiation and diurnal cycle radiation. Section 5 provides a summary and
113 discussions.

114

115 **2. Data and method**

116 **2.1 ICOADS and ERA5**

117 We employ shipborne observations provided by the International Comprehensive
118 Ocean–Atmosphere Data Set (ICOADS) to investigate the occurrence of sea fog over
119 the summer NWP. Fog is identified when the present-weather code is between 10 and
120 12 or between 40 and 49, and the visibility is lower than 1 km (Bari et al., 2016; Yang
121 et al., 2021). Additionally, we also use SST, SAT, and 10 m winds to examine the sea-
122 air interface conditions during sea fog. We include $\sim 6 \times 10^4$ fog reports over the NWP
123 between 1998 and 2018 to explore sea fog climatologies and select a fog case that took
124 place during 1- 4 July 2013 for further analysis and simulation.

125 To construct the idealized initial conditions for the sea fog simulation, we use the

126 fifth generation of the European Centre for Medium-Range Weather Forecasts
127 atmospheric reanalysis (ERA5, Hersbach et al., 2020). ERA5 fields are on a $0.25^\circ \times$
128 0.25° grid with 16 levels below 500 hPa.

129 **2.2 UCLA-LES model**

130 UCLA-LES is a three-dimensional, turbulence-closure boundary layer model with
131 prognostic variables such as total water mixing ratio q_t , liquid water potential
132 temperature θ_l , and three components of wind. This model is often used to simulate
133 stable, neutral, and convective boundary layers (Stevens et al., 2005).

134 The parameterization for subgrid fluxes in UCLA-LES is based on the
135 Smagorinsky–Lilly model (Smagorinsky, 1963; Lilly, 1967) to satisfy the model
136 closure. This model can explicitly compute thermal turbulent flux and appropriately
137 describe turbulent mixing process within the boundary layer (Stevens et al., 2005; Jiang
138 et al., 2006). Surface fluxes of momentum, temperature, and moisture are computed
139 based on similarity theory (Stevens et al., 2010). We set specific surface properties to
140 represent oceanic conditions and prescribe surface temperature and specific humidity.
141 Radiative transfer calculations are performed using the δ -four-stream method (Fu and
142 Liou, 1993; Pincus and Stevens, 2009), and radiative fluxes are based on background
143 profiles of pressure, temperature, humidity, and ozone content (Stevens et al., 2003).
144 The model has a warm-rain microphysical scheme (Seifert and Beheng, 2001) assuming
145 that cloud droplets are in equilibrium at a fixed concentration. The microphysics
146 process accounts for the interactions within the same type and between different types
147 of cloud and raindrops. We set a specified $100 \times 10^6 \text{ g kg}^{-1}$ cloud-droplet mixing ratio in
148 our simulations. To capture the delicate radiative and turbulent processes, we set
149 horizontal grid spacing as 20 m and the vertical grid spacing as 1 m below 50 m and 5
150 m above 50 m. The simulation domain is $1500 \text{ m} \times 1500 \text{ m} \times 2000 \text{ m}$.

151 **2.3 Diagnostic equations**

152 We analyze the budget of domain-averaged heat and water vapor to investigate the
153 related physical processes responsible for sea fog evolution. The heat budget is
154 calculated using

155
$$\frac{\partial \bar{\theta}}{\partial t} = -\frac{\partial \overline{w'\theta'}}{\partial z} - \frac{L_v E}{\bar{\rho} c_p} - \frac{1}{\bar{\rho} c_p} \frac{\partial \bar{Q}}{\partial z}, \quad (1)$$

156 where θ is potential temperature. The term on the right-hand side (RHS) describes the
 157 heat change from turbulent mixing, latent heat releasing, and the radiation effect,
 158 **respectively.** $\overline{w'\theta'}$ is the sum of resolved and sub-scale parameterized turbulent heat
 159 flux. **E is the amount of water vapor produced by liquid phase transition.** L_v is the latent
 160 heat release of condensation or evaporation. ρ is air density. $C_p = 1004.67 \text{ J kg}^{-1} \text{ K}^{-1}$ is
 161 specific heat of moist air. Q is radiation flux. The water vapor budget equation is

162
$$\frac{\partial \bar{q}_v}{\partial t} = -\frac{\partial \overline{w'q'_v}}{\partial z} + \frac{E}{\bar{\rho}}, \quad (2)$$

163 where q_v is water vapor mixing ratio. The terms on the RHS describe the q_v change from
 164 turbulent mixing effect and evaporation/condensation. $\overline{w'q'_v}$ is the sum of resolved and
 165 sub-scale turbulent water vapor flux.

166 To diagnose the turbulent mixing process responsible for heat and **moisture** variation,
 167 we compute the turbulent kinetic energy (TKE) budget using

168
$$\frac{\partial \overline{TKE}}{\partial t} = +\frac{g}{\theta_v} \left(\overline{u'_3 \theta'_v} \right) - \overline{u'_i u'_3} \frac{\partial \bar{u}_i}{\partial x_3} - \frac{\partial (\overline{u'_3 TKE})}{\partial x_3} - \varepsilon, \quad (5)$$

169 where subscripts $i = 1, 2,$ and 3 represent $x, y,$ and z coordinates. The four terms on the
 170 RHS represent buoyancy production, mechanical production from wind shear, the
 171 vertical transport of TKE, and TKE dissipation due to friction, respectively.

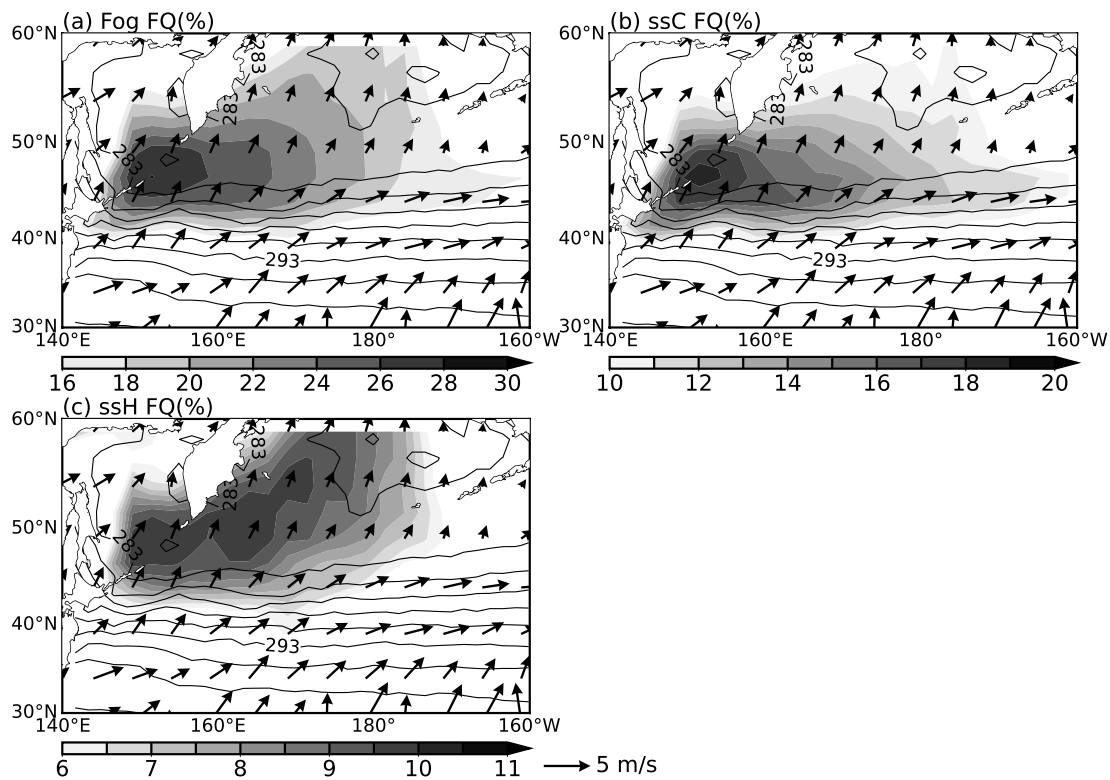
172

173 **3. Advection fog with ssH in ICOADS observations**

174 **3.1 Statistical features of ssH fog**

175 To isolate advection fog, we trace back each ICOADS fog observation for 48 hours
 176 **by integrating ERA5 winds at 10 m.** **We define the fog observations from warmer waters**
 177 **as advection fog in this study and obtain 43,105 advection fog observations during the**
 178 **period of 1998-2018.** **Figure 1 shows the climatological frequency of advection fog,**
 179 **advection fog with sea surface cooling (ssC, when SAT-SST > 0), and advection fog**
 180 **with ssH over the NWP during June-July-August (JJA).** Advection fog is frequently
 181 observed on the cold flank of the Kuroshio Extension front, with a peak frequency of
 182 ~30% near the Kuril Islands, where intense tidal mixing results in SSTs below 10°C

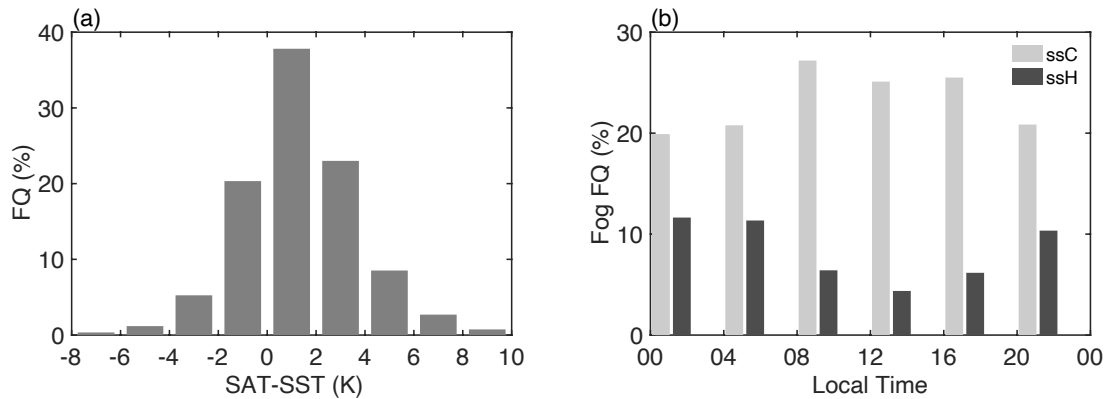
183 (Fig. 1a; Tokinaga and Xie, 2009). Advection fog with ssC primarily appears in a band-
 184 shaped region between 40°N and 52°N, a distribution similar to that of all advection
 185 fog (Figs. 1a and b). The frequency of ssH fog also peaks at ~10% near the Kuril Islands
 186 (Fig. 1c), but its region of maximal occurrence extends further downstream to the north
 187 of 52°N. A detailed comparison of Figs. 1a and 1b suggests that approximately half of
 188 the ssC fog transitions into ssH fog as the fog column migrates northward under
 189 prevailing southwesterlies.



190
 191 FIG. 1 Climatological SST (contours with 2-K intervals), surface winds (vectors, $m s^{-1}$), and frequencies
 192 (shading, %) of (a) advection fog, advection fog with (b) ssC and (c) ssH during June-July-August for
 193 1998-2018. The SST and winds are based on ERA5, and the fog frequencies are obtained from ICOADS.

194 Figure 2 illustrates the probability density function (PDF) of simultaneous SAT-
 195 SST values concurrent with advection fog over the NWP during JJA. The majority of
 196 these SAT-SST values are positive (Fig. 2), consistent with the observational results of
 197 Fu and Song (2014). However, a substantial proportion (~27.5%) of advection fog in
 198 the NWP is associated with ssH fog. Based on coastal buoy observations, Yang et al.
 199 (2019) reported that ~30% of SAT falls below SST during fog events in the Yellow Sea.
 200 Li et al. (2022) also observed ~32% fog is with ssH over the northeast Pacific during
 201 winter. The consistent observations of advection fog with ssH imply that cooling

202 mechanisms other than near-surface turbulent cooling have a substantial impact on the
 203 evolution of advection fog.



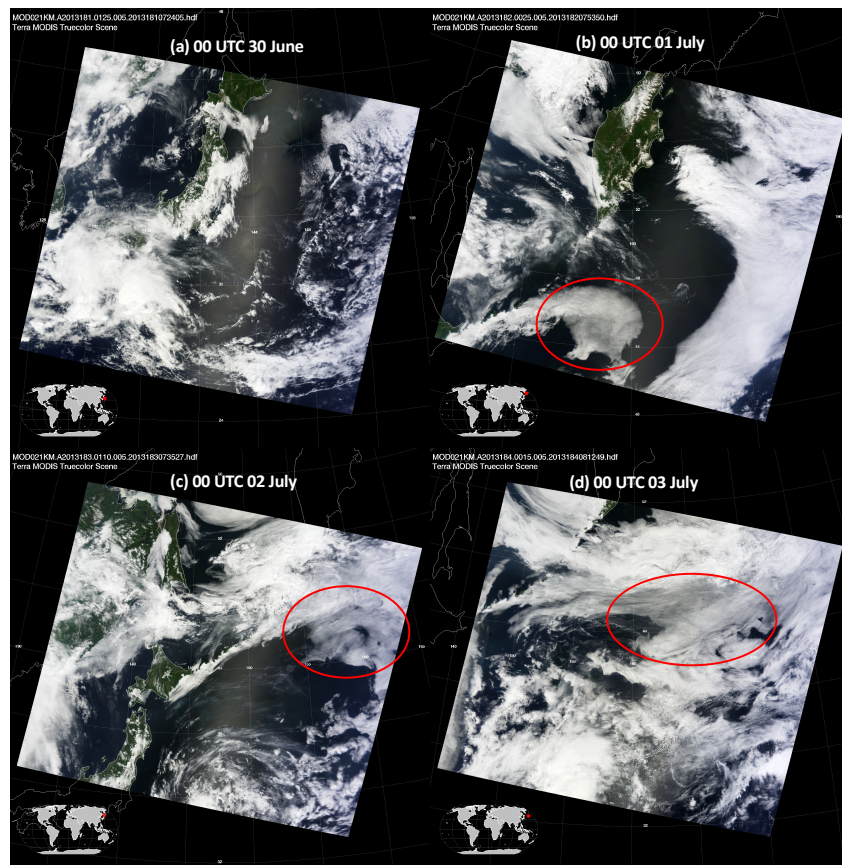
204
 205 FIG. 2 (a) Probability density function (%) of SAT-SST ($^{\circ}\text{C}$) concurrent with advection fog
 206 observations over the NWP ($30\text{-}60^{\circ}\text{N}$, $140\text{-}200^{\circ}\text{E}$) during June-July-August based on ICOADS. (b)
 207 The frequencies of advection fog with ssH (dark grey bars) and ssC (light grey) as functions of local
 208 time.

209 There is a noticeable diurnal variation in ssH fog over the NWP (dark grey bars in
 210 Fig. 2b). Local time is determined based on the universal time of fog observations and
 211 their respective longitudes. The frequency of ssH fog reaches its maximum ($\sim 11.5\%$)
 212 and minimum ($\sim 4\%$) during 0000-0400 and 1200-1600 local time, respectively (the
 213 dark grey bars in Fig. 2b). Relative to all advection fog occurrences, the frequency of
 214 ssH fog is $\sim 18.8\%$ during the daytime and increases to $\sim 34.5\%$ at night. In contrast, the
 215 frequency of ssC fog is highest around sunrise (the light grey bars in Fig. 2b) and does
 216 not exhibit a clear diurnal variation. The evident diurnal cycle of ssH fog over the open
 217 sea is new to our knowledge and suggests that the radiative balance over fog top
 218 significantly alters the evolution of advection fog.

219 3.2 An ssH fog case

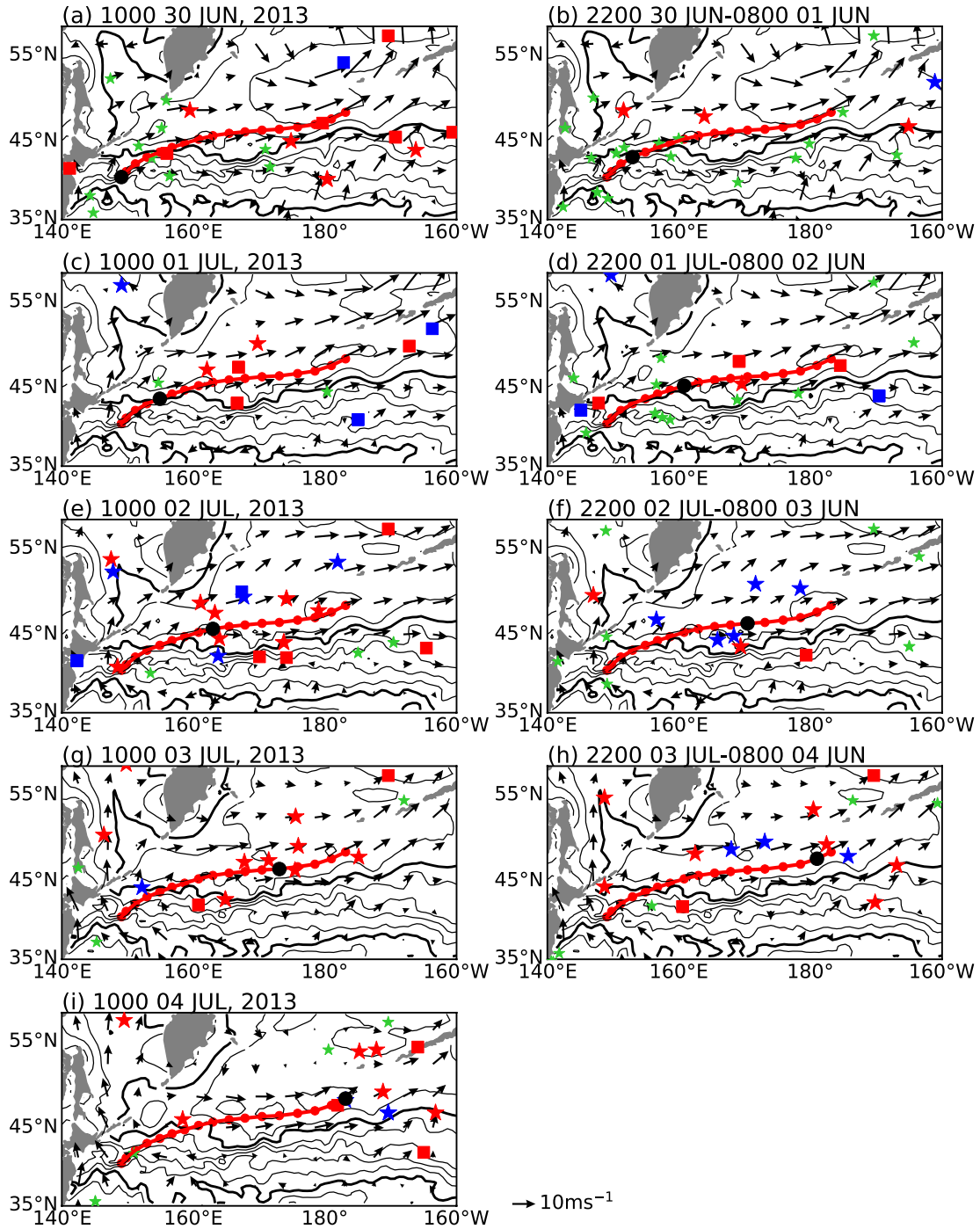
220 We examine an advection fog event during 01- 04 July 2013 over the NWP.
 221 Satellite images observed by the Moderate Resolution Imaging Spectroradiometer
 222 (MODIS) captured clear fog patches at 1000 local standard time (LST) 01-03 July near
 223 the Kuril Islands and over the northwest Pacific (Fig. 3b). The synoptic steady
 224 southwesterlies over the SST front caused the fog event (Fig. 4), and ICOADS
 225 observations reported no precipitation during this period. Further information regarding
 226 this fog event can be found in Yang et al. (2021). Our primary focus is on the negative

227 SAT-SST observations during this fog episode (Fig. 4). Fog was first reported near the
228 Kuril Islands at the night of 30 June (red stars in Figs. 2b), concurring with positive
229 SAT-SST. The southwesterly winds, along with positive SAT-SST, signify the event as
230 advection fog. As the saturated air moved northeastward (Figs. 3b-d and 4e-h), negative
231 SAT-SST was detected within the fog patch during 02-04 July (blue stars in Figs. 4e-h).
232 Notably, most of the ssH fog occurred at night. Figure 5 shows the time series of
233 observational SAT-SST closest to the trajectory in Fig. 4. After fog formation, there is
234 a noticeable diurnal variation in the sea-air temperature difference, with air temperature
235 dropping below SST during the nights of 02 and 03 July. The minimum sea-air
236 temperature difference reaches -1 K at 2200 LST on 03 July.



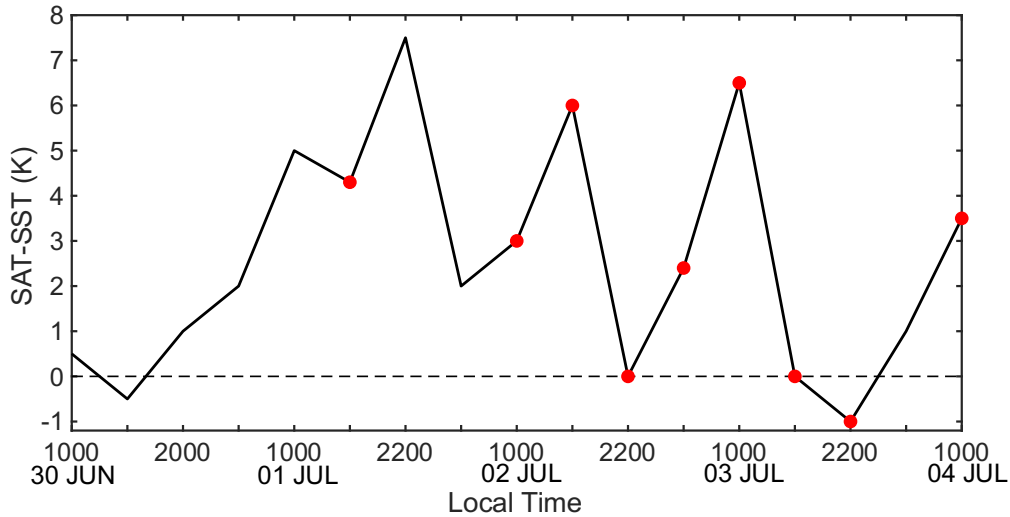
237

238 FIG. 3 Visible satellite images from MODIS.



239

240 FIG. 4 ICOADS observations of the advection fog event during 30 June - 04 July, 2013. The blue and
 241 red stars represent ssH and ssC fog, respectively, and squares indicate stratus, and green stars indicate
 242 other cloud types or clear sky. The ICOADS observations and ERA5 10-m winds near 1000 LST from
 243 30 June to 04 July are shown in (a), (c), (e), (g), and (i), respectively. The ICOADS reports and ERA5
 244 winds between 2200-0800 (+1 day) LST are shown in (b), (d), (f), (h), respectively, to include more
 245 nighttime observations. The thick red line in each panel demonstrates the 4-day back trajectory from the
 246 ssH fog observation at 49.6°N 183.2°E, and the red dots are the location of the trajectory every 6 hours,
 247 and larger black dot indicating the location at the corresponding time of the panel. The contours are
 248 averaged ERA5 SSTA during 30 June-04 July, and the thick contours indicate 283, 293 and 303 K,
 249 respectively.



250

251 FIG. 5 ICOADS observations of SAT-SST closed to the trajectory in Fig. 4. The red dots indicate fog
 252 occurrences.

253 4 Simulation with constant solar radiation

254 4.1 Simulation setups

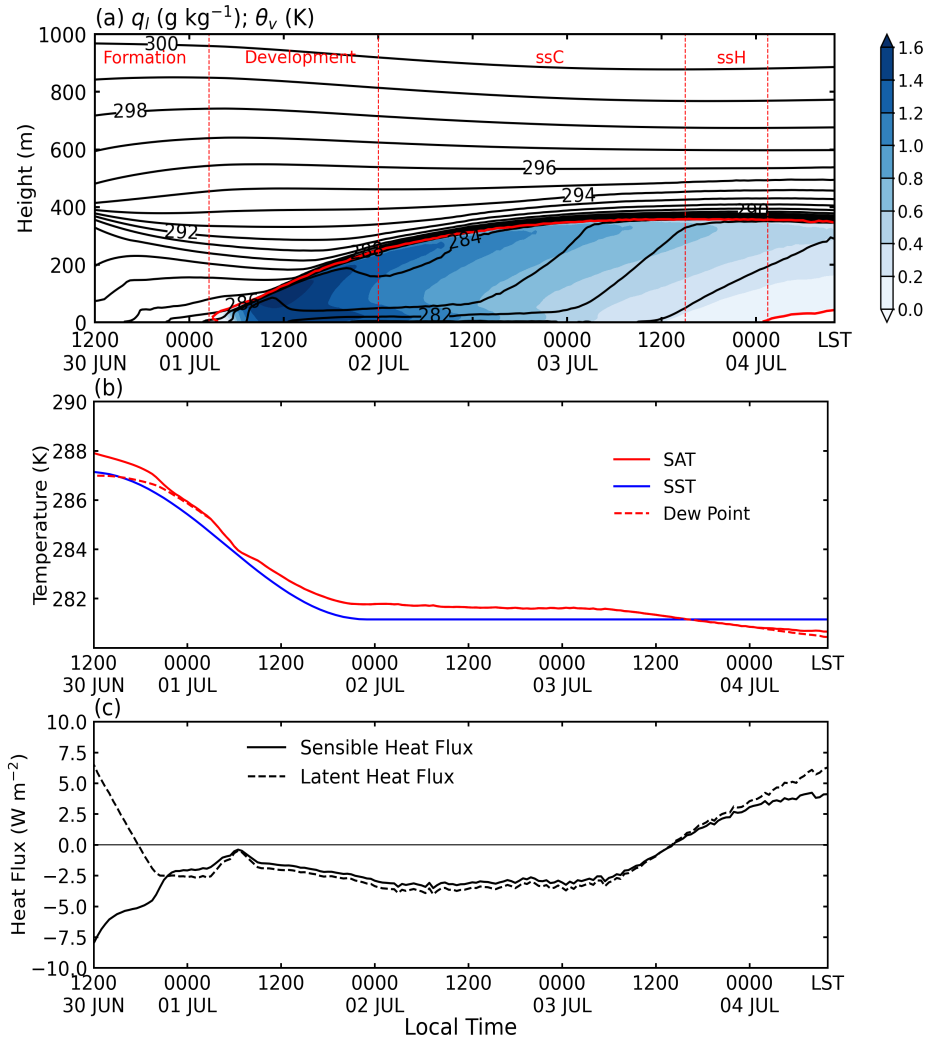
255 The synoptic processes associated with the fog event detailed in subsection 3b
 256 align closely with the climatological characteristics of ssH and ssC fog (Figs. 1 and 2).
 257 To uncover the boundary-layer processes responsible for the ssH fog, we use the
 258 UCLA-LES model to simulate this typical fog event from a Lagrangian perspective.
 259 We trace back an ssH fog observation at 49.6 °N 183.2 °E in Fig. 4i, which had an SAT-
 260 SST value of -1.2 °C. This trajectory is roughly consistent with the one obtained using
 261 HYSPLIT trajectory model (Draxler and Rolph, 2010; not shown). The air column
 262 consecutively experienced no fog, ssC, and ssH fog along the trajectory from 30 June
 263 to 04 July, 2013 (Figs. 4 and 5).

264 We prescribe time-varying SST and large-scale divergence to force the boundary
 265 layer evolution. To fit the observations, we simplify the observational SST by
 266 employing a cosine function during the initial 36 h, succeeded by a constant value of
 267 8 °C (not shown). The fog case and the simulation setups are the same as those in Yang
 268 et al. (2021), except for the divergence forcing in the free-atmosphere. We apply a
 269 realistic divergence of $2 \times 10^{-6} \text{ s}^{-1}$, which is the averaged value along the trajectory and
 270 is double the climatological value in Yang et al. (2021). We first perform a simulation
 271 with fixed solar radiation.

272 We generate idealized initial conditions for the simulation by integrating ERA5
273 and satellite data. Cloud–Aerosol Lidar and Infrared Pathfinder Satellite Observations
274 (CALIPSO) indicated a boundary layer height of 400 m (not shown). We establish a
275 typical clear-sky boundary layer structure by linearizing the original ERA5 profiles into
276 three parts: The mixed layer, inversion, and free troposphere. Within the 400 m deep
277 mixed layer, θ and q_l profiles remain constant (Figs. 7a and b). Above the mixed layer,
278 an inversion with a 6 K jump in θ is present (Fig. 7a). In the free troposphere, θ and q_l
279 decrease at the rate of -6.6 K km^{-1} (Fig. 7a) and $-4 \text{ g kg}^{-1} \text{ km}^{-1}$ (Fig. 7b), respectively.
280 Throughout the simulation, winds of 9.6 m s^{-1} in geostrophic balance are applied.

281 4.2 Evolution in boundary-layer structure

282 Figure 6a depicts the time-height section of liquid water mixing ratio (q_l) and
283 virtual potential temperature (θ_v) for the air column in the simulation with constant solar
284 radiation. We exclude the first 2 hours of results due to the model's spin-up. Liquid
285 water initially appears near surface ($\sim 20 \text{ m}$) at 0400 local standard time (LST) 01 July
286 and rapidly extends to the surface within 1 h, resulting in fog formation. We define fog
287 when q_l exceeds 0.02 g kg^{-1} (Kunkel, 1984). Fog persists until 0200 LST on 4 July,
288 transitioning into stratus as the near-surface droplets evaporate. This transition results
289 from the entrainment of the free-atmospheric dry air caused by the fog-top LWC (Yang
290 et al., 2021). The height of the fog top grows from 20 to 380 m until 0000 LST 03 July
291 and rarely varies thereafter. CALIPSO passed through the fog area and observed cloud-
292 top heights of about 300 m and 400 m on 0000 LST 02 July and 0100 LST 03 July (not
293 shown), respectively, which is very close to simulated results. The capping inversion
294 intensifies from 5 to 12 K after fog formation due to the fog layer cooling (Fig. 5a).



295

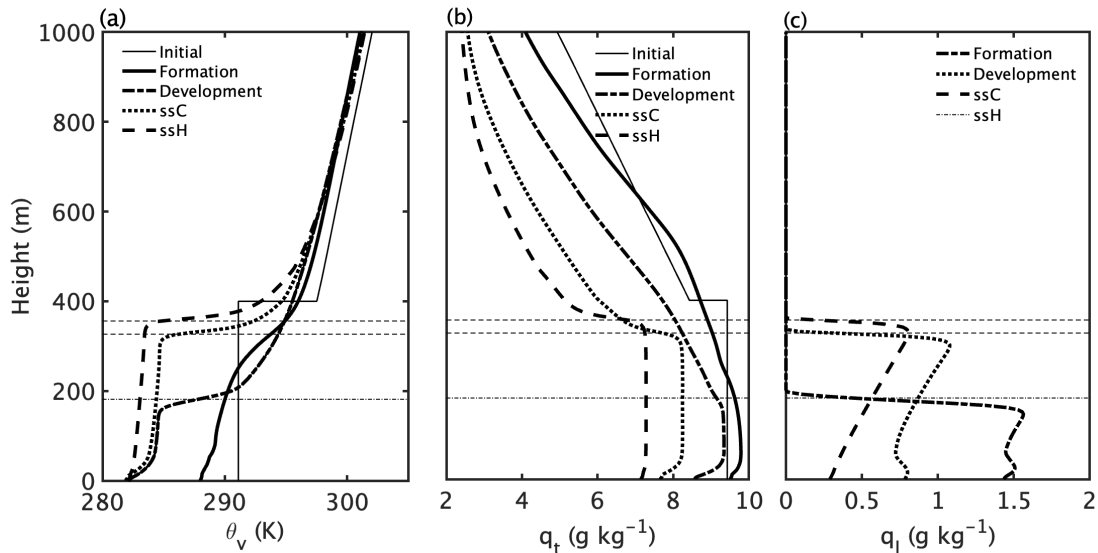
296 FIG. 6. (a) Time-height section of simulated liquid water mixing ratio (shading, $g\ kg^{-1}$), virtual potential
 297 temperature (contours, K) for constant solar radiation simulation. Red lines indicate the fog/cloud top
 298 and bottom, respectively. (b) SAT (red line, K), SST (blue, K) and surface dewpoint temperature (dashed
 299 red, K). (c) Same as (b) but for surface sensible heat flux (solid, $W\ m^{-2}$) and latent heat flux (dashed, $W\ m^{-2}$). Upward
 300 sensible and latent heat fluxes are positive. Red dashed lines in (a) divide the evolution
 301 process of fog into the four phases described in the article.

302

303 The model successfully reproduces the ssH fog. Over the SST front, SAT follows
 304 the underlying SST with a difference of 0.8 K, resulting in strong downward sensible
 305 heat flux between -7.5 and $0\ W\ m^{-2}$ (Figs. 6b and 6c). At 0400 LST on 01 July, SAT
 306 drops to the dewpoint at 285.8 K. After crossing the SST front, SAT is almost constant
 307 during the period of 0000 LST on 02-03 July but quickly decreases afterward, falling
 308 below SST at 1700 LST on 03 July (Fig. 6b). The occurrence time of ssH fog is
 309 consistent with ICOADS observations. The minimum air-sea temperature difference
 during sea fog is $-0.65\ K$, weaker than the observed $-1\ K$ (Figs. 5 and 6b). From this

310 time, both sensible and latent heat fluxes change their directions, indicating that the
 311 ocean begins to heat and moisten the surface air (Figs. 5b and 5c). The ssH fog sustains
 312 for 12 hours.

313 We divide the simulation into four phases: fog formation (from 1200 LST on 30
 314 June to 0400 LST on 01 July) and development (from 0400 LST on 01 July to 0000
 315 LST on 02 July) over the SST front, followed by fog maintenance with ssC (from 0000
 316 LST on 02 July to 1700 LST on 03 July) and ssH (from 1700 LST on 03 July to 0200
 317 LST on 04 July) to the north of the SST front. Figure 6 shows boundary layer structure
 318 for the above four phases. The soundings of θ_v , total water mixing ratio (q_t), and q_l are
 319 domain-averaged at the selected times.



320
 321 FIG. 7. Horizontal mean soundings for constant solar radiation simulation at 1000 LST on 30 June (thin
 322 solid line), 2000 LST on 30 June (solid), 1200 on LST 01 July (dot-dashed), 1200 LST on 02 July (dot)
 323 and 2000 LST on 03 July (dashed). (a) Virtual potential temperature (K), (b) total water mixing ratio (g
 324 kg^{-1}) and (c) liquid water mixing ratio (g kg^{-1}). Horizontal dot-dashed line represents fog top height at
 325 1200 on 01 July, and the horizontal dashed line represents fog top heights at 1200 on 02 July and 2000
 326 on 03 July.

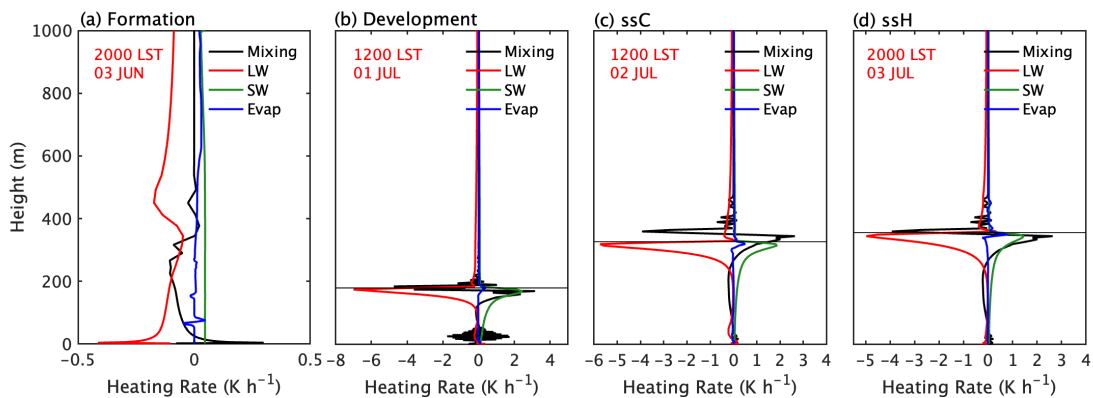
327 Before fog formation, the cold sea surface efficiently cools the near-surface air,
 328 creating a stable boundary layer (Figs. 6a and 7a). q_t increases with height below 20 m
 329 and remains nearly constant within the boundary layer (Fig. 7b). The upward decrease
 330 in air temperature and increase in q_t result in the maximal relative humidity and
 331 saturation occurring near 20 m (Fig. 7a). Once fog forms, a mixed layer develops
 332 downward from the fog top to 50 m, capping the original stable layer produced by the

333 cold sea surface (Fig. 7a). θ_v and q_t of the boundary layer decrease by ~ 6 K and ~ 1 g
 334 kg^{-1} , respectively, from 2000 LST on 30 June to 1200 LST on 01 July (Figs. 7a and 7b).
 335 Large q_t near fog top converses into rainwater and descends, resulting in a secondary
 336 peak of q_t near the surface at about 20 m (Fig. 7c). The stratifications of θ_v , q_t and q_l
 337 indicate a different cooling mechanism at the fog top from that at its bottom (Fig. 7a).

338 During the ssC fog phase, a well-mixed boundary layer develops, and θ_v decreases
 339 by 1 K from 1200 LST on 01 July to 1200 LST on 02 July (Figs. 7a and 7b). q_t peaks
 340 near the fog top (Fig. 7c). During the ssH fog phase, the sea surface heats and moistens
 341 the fog layer (Fig. 6b), while the fog layer keeps cooling and drying at a much slower
 342 rate (Fig. 7a), indicating that the LWC effect at the fog top dominates the fog cooling
 343 and maintenance. The thermal and moisture stratifications of ssH fog share a similar
 344 structure to those of ssC fog but with a deeper well-mixed layer (the long dashed lines
 345 in Fig. 7).

346 4.3 Heat and moisture budgets

347 Figure 8 shows the profiles of heat and water vapor budget terms at different
 348 phases. Figures 9a and 9b show the time series of surface heat and water vapor budget
 349 terms, respectively. Over the SST front, the turbulent mixing and longwave radiation
 350 effects cool the air both near the surface and throughout the entire boundary layer (Figs.
 351 8a and 9a). Fog forms due to the cooling of the air near the surface (Fig. 8a).

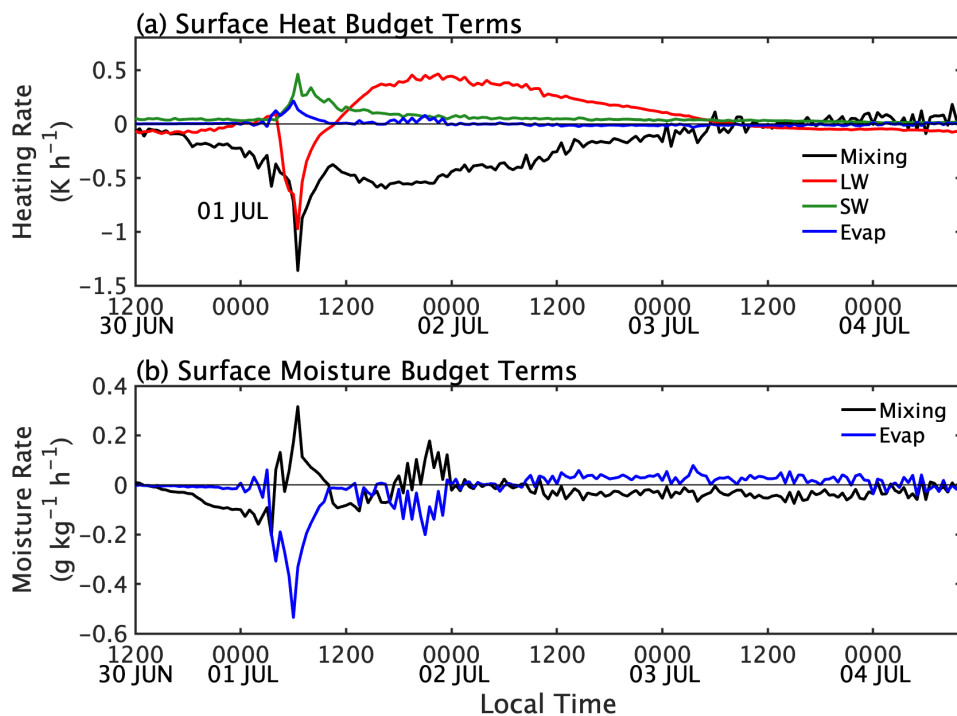


352
 353 FIG. 8 Profiles of horizontal mean budget terms for heat (K h^{-1}) at (a) 2000 LST on 30, (b) 1200 LST on
 354 01 July, (c) 1200 on 02 July and (d) 2000 LST on 03 July in the constant solar radiation simulation. The
 355 horizontal lines indicate fog tops.

356 After fog formation, the surface turbulent cooling intensifies dramatically, peaking
 357 at -1.35 K h^{-1} , leading to a marked decrease in SAT (Fig. 9a). The rapid growth of q_t

358 releases latent heat through condensation, which partly offsets the cooling effect from
 359 turbulent mixing. Caldwell and Bretherton (2005) suggested that sedimentation has a
 360 drying and heating effect on the surface layer. The impact of sedimentation for the heat
 361 budget is relatively small compared to turbulent mixing and LWC, both at the surface
 362 and within the boundary layer (not shown). Within the boundary layer, longwave
 363 radiation effect induces strong cooling at the fog top, and the resultant turbulent mixing
 364 cools the upper boundary layer (the red line in Fig. 8b). Additionally, thermal turbulence
 365 helps entrain the warm, dry air from the free atmosphere, warming the air at the fog top
 366 while cooling the air above the fog layer (the black line in Fig. 8b).

367 When the fog volume moves north of the SST front (0000 LST on 02 July onward),
 368 the surface cooling effects become weak due to the fixed SST and turbulent mixing
 369 keeps drying the surface air (Fig. 9). Strong LWC persists at the fog top, inducing
 370 turbulent mixing that cools the entire fog layer (Figs. 7a and 8c). In this case, the effect
 371 of the fog-top LWC overcomes the surface cooling effect, causing SAT to drop below
 372 SST. During the ssH phase, the LWC at the fog top slightly weakens and the turbulent
 373 mixing cooling dominates within the fog layer, causing SAT to continuously decrease
 374 (Figs. 6b and 8d).

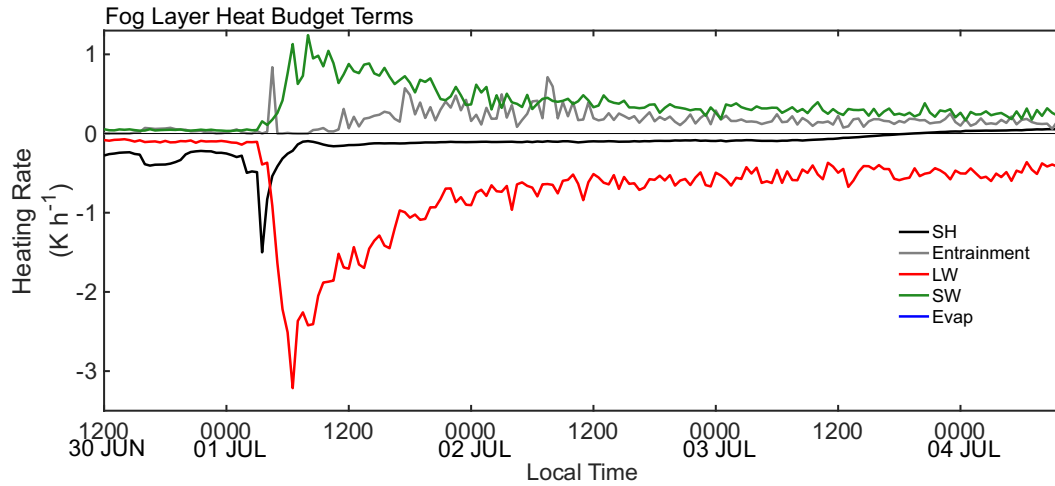


375
 376 FIG. 9 Time series of horizontal mean budget terms at the surface for the constant solar radiation

377 simulation: (a) heat (K h^{-1}) and (b) water vapor ($\text{g kg}^{-1} \text{ h}^{-1}$).

378 We quantify the heat budget for the fog layer by integrating heat budget for the fog
379 layer (Fig. 10). We determine the turbulent mixing term by calculating the difference
380 between the turbulent heat fluxes at the surface ($\overline{w'\theta'}_{sfc}$) and fog top ($\overline{w'\theta'}_{zi}$, z_i is fog
381 top height), representing the surface sensible heat transport and the effect of the fog-top
382 entrainment, respectively (the black and grey lines in Fig. 10). Prior to fog formation,
383 the surface sensible heat transport drives the boundary layer cooling (the black line in
384 Fig. 10). After the fog forms, the effect of longwave radiation acts to cool the boundary
385 layer due to the longwave heat loss at fog top (the red line). The LWC effect rapidly
386 exceeds surface cooling 2 hours after fog formation. Both shortwave radiation and
387 entrainment at the fog top warm the fog layer, partially offsetting the effects of surface
388 cooling and LWC.

389 The normalized LWC by the fog layer depth peaks 6 hours after fog formation and
390 then decreases rapidly (Fig. 10). This is possibly related to a negative feedback between
391 the fog-top radiative cooling and entrainment (Gerber et al. 2013, 2014). Following the
392 fog formation, an increase in fog-top entrainment causes a reduction in the liquid water
393 gradient at the fog top, which subsequently reduces the radiative cooling. This negative
394 feedback process takes several hours to take effect (not shown). Another reason for the
395 initial surge in LWC is the rapid growth of fog layer depth. In addition, we examine the
396 time-series maximum in LWC profiles (not shown), which fluctuates around 8 K h^{-1}
397 after fog formation and then steadily decreases. The fog-top LWC is somewhat less than
398 the counterpart for typical stratocumulus clouds (Curry and Herman 1985; Gerber et al.
399 2014). This may be attributed to the difference in free atmospheric humidity between
400 fog and stratocumulus scenes. In the case of stratocumulus clouds, the corresponding
401 descending motion results in drier air compared to the free atmosphere above fog. As
402 the fog moves to the cold flank of the SST front, the surface cooling weakens and
403 reverses, slightly heating the fog layer after SAT drops below SST. Overall, the
404 persistent and strong LWC at the fog top dominates the fog evolution, resulting in the
405 ssH fog.

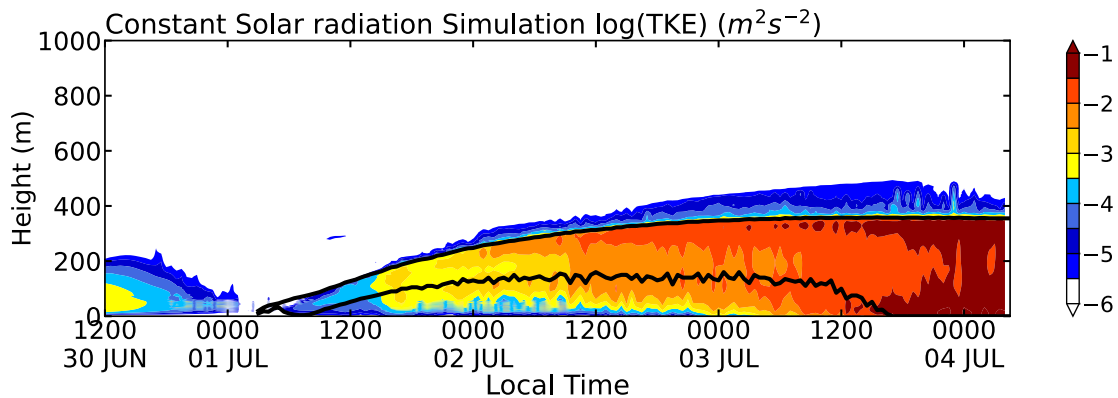


406

407 FIG. 10 Time series of horizontal mean heat budget terms (K h^{-1}) of the integral boundary layer for the
 408 constant solar radiation simulation.

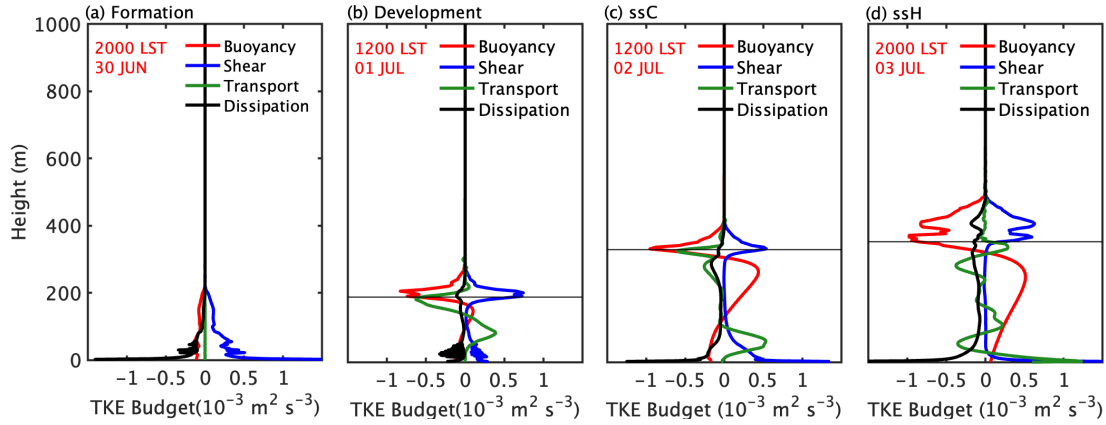
409 **4.4 TKE and its budget**

410 Figure 11 presents the time-height cross section of TKE for the simulation with
 411 constant solar radiation. Prior to fog formation (0400 LST on 01 July), TKE exhibits a
 412 relatively low magnitude below 200 m (Fig. 11), produced by the near-surface wind
 413 shear and dissipated by friction and buoyancy (Fig. 12a). Mechanical turbulence
 414 facilitates the transport of cooling from the surface, contributing to the fog formation.
 415 Following fog formation, the LWC at the fog top induces buoyancy production of
 416 turbulence over the upper boundary layer (Fig. 12b), leading to a noticeable peak in
 417 TKE near the fog top ~ 12 hours after its formation (Fig. 11).



418

419 FIG. 11 Time-height section of $\log_{10}(\text{TKE})$ (shading in $\text{m}^2 \text{s}^{-2}$), and time series of fog/cloud top height
 420 (upper black lines in m) and thermal turbulence interface (lower black lines in m) for the simulations
 421 with constant solar radiations.



422
423 FIG. 12 Profiles of horizontal mean TKE budget terms ($10^{-3} \text{ m}^2 \text{ s}^{-3}$) for the constant solar radiation
424 simulation at (a) 2000 LST on 30 June, (b) 1200 LST on 01 July, (c) 1200 LST on 02 July and (d)
425 2000 LST on 03 July. Thin black lines indicate fog tops.

426 Turbulence in the ssC fog intensifies after its formation at 0000 LST on 02 July
427 (Fig. 11). The terms in TKE budget also exhibit a general strengthening trend from fog
428 formation to the ssC fog (Fig. 12c). The generation of buoyancy-driven turbulence
429 enhances and develops downward, leading to a deeper mixing layer within the boundary
430 layer and cooling fog layer (Figs. 7a and 12c). TKE exhibits a significant increase from
431 the ssC fog to ssH fog, particularly near the surface. This is because the air-sea interface
432 becomes unstable ($\text{SAT-SST} < 0$), leading to the buoyancy production of turbulence
433 (Fig. 12d). During this period, both buoyancy-induced and mechanically-induced
434 turbulence contribute significantly to the maximum TKE near the surface.

435 The vertical structure of turbulence can be elucidated by employing the thermal
436 turbulence interface, which distinguishes between the layers characterized by thermal
437 and mechanical turbulence (Huang et al., 2015). Huang et al. (2005) defined a thermal
438 turbulence interface as the gradient of the observational potential pseudo-equivalent
439 temperature equals zero. Thermal turbulence induced by LWC is prevalent above the
440 thermal turbulence interface, which is static unstable, whereas mechanical turbulence,
441 aroused by wind shear, is predominant below the interface. Thermal turbulence
442 interface helps to separate the fog layer into zones dominated by LWC and surface
443 cooling. In this article, thermal turbulence interface is defined as the lowest altitude
444 within the fog layer where the buoyancy production of turbulence is positive (the black
445 lines in Fig. 11). Following fog formation, a thermal-turbulence mixing layer forms

446 beneath the fog top and extends across the upper half of the fog layer from 0000 LST
447 on 02 July (Fig. 11). After 0000 LST on 03 July, the mixing layer continues to develop
448 downward, eventually reaching the sea surface by 1500 LST on the same day, thus
449 establishing a well-mixed boundary layer. Subsequently, the thermal turbulence cools
450 the near-surface air and causes SAT to drop below SST after a 2-hour interval (Fig. 6b).

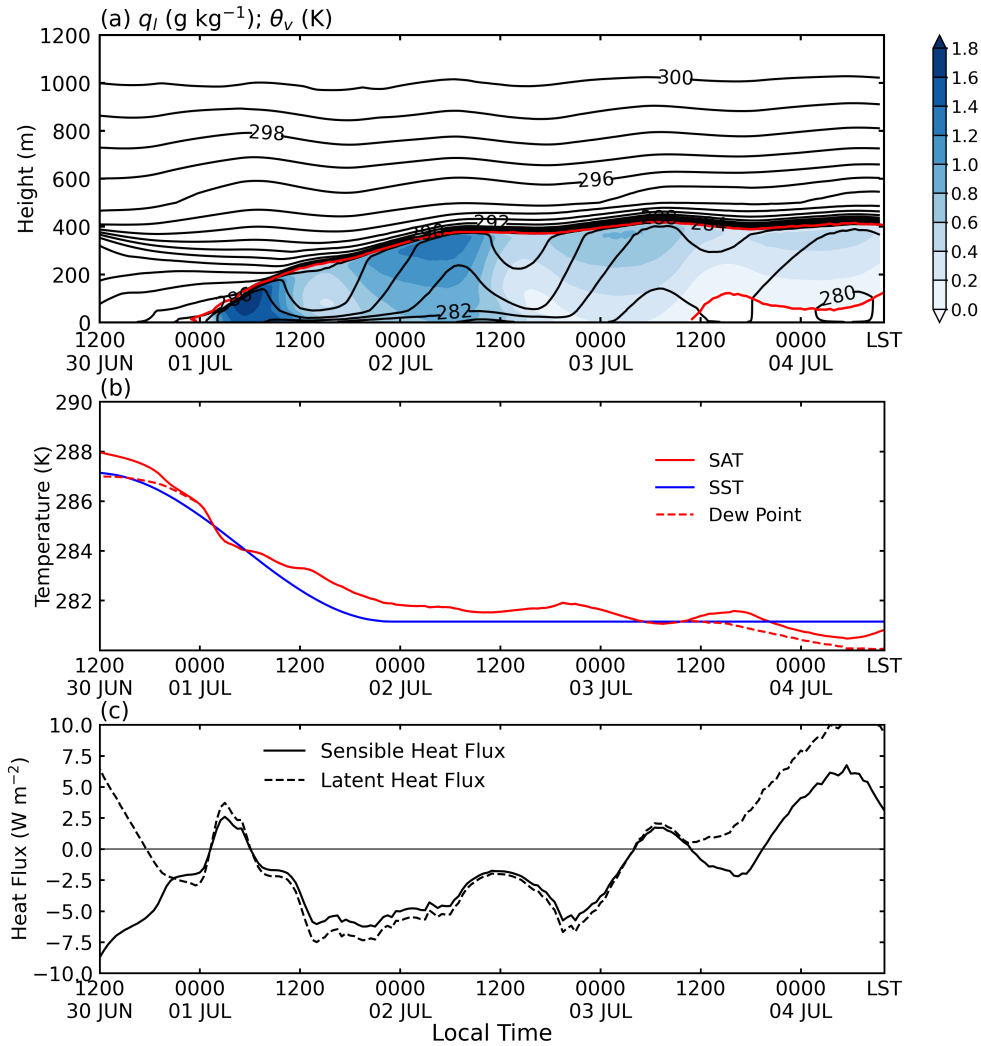
451 **5 Simulation with diurnal solar radiation**

452 We conduct an additional simulation that incorporates diurnal solar radiation.
453 Overall, the simulated fog with diurnal solar radiation exhibits similar behavior to that
454 in the simulation with constant solar radiation, but with clear diurnal variations. Fog
455 forms at 2200 LST on 30 June and rapidly grows. During the night, the stronger fog-
456 top LWC enhances thermal turbulence and entrainment, causing an increase in the fog
457 top height (Fig. 13a). In contrast, during the day, fog height decreased noticeably (Fig.
458 13a). With the continued drying effect of entrainment, liquid water content in the fog
459 layer decreases, ultimately causing the transition from fog to stratus at 1100 LST on 03
460 July (Fig. 13a).

461 The simulation incorporating diurnal solar radiation also generates ssH fog, which
462 exhibits significant diurnal variation. During the nights of 03 July and 04 July, SAT
463 rapidly drops below SST after sunset and recovers above SST after sunrise, which is
464 similar to the variations of observational SAT-SST (Figs. 5 and 13b). This result
465 indicates that the diurnal variation in the radiative balance over the fog top considerably
466 alters the transitions between ssC and ssH fog. The LWC at fog top has a clearer diurnal
467 variation and dominates the air-sea temperature differences (not shown). About 3-5
468 hours before sunset, the fog top LWC reach its minimum during a day. The
469 enhancement of LWC occurs approximately 3 hours earlier than the decline in air-sea
470 temperature difference, ultimately causing the air temperature falls below SST in the
471 early hours of 03 July (not shown). Additionally, both TKE and thermal-turbulence
472 mixing layer exhibit distinct diurnal variations (Fig. 14). The pronounced radiative
473 cooling at the fog top results in increased TKE and a thicker thermal-turbulence mixing
474 layer at nighttime compared to daytime (Fig. 14). The time period when the mixing

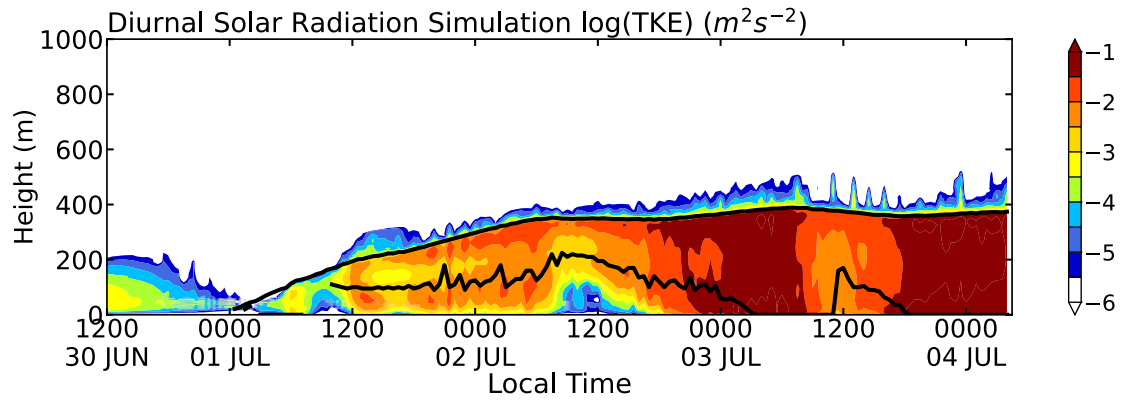
475 layer base and the ground coincide is the same as the occurrence period of ssH fog,
 476 further demonstrating the regulating effect of LWC on the fog layer cooling.

477 We also conducted a simulation with intensified solar irradiance through an
 478 increase in solar elevation angle to check the effect of solar irradiance. Sea fog
 479 dissipates 8 hours earlier than that in the standard solar radiation experiment and
 480 observations (not shown). Two hours before sea fog dissipation, there is the ssH fog
 481 occurrence. Nevertheless, there are minimal changes in the evolution of the fog top
 482 height and the thermal and dynamic structure of the boundary layer during sea fog.



483

484 FIG. 13 As in Fig. 6, but for the simulation with diurnal cycle radiation.



485

486 FIG. 14 As in Fig. 11, but for the simulation with diurnal cycle radiation.

487 6 Summary and discussion

488 Sea fog is of great importance due to its significant impact on maritime activities.
 489 The present study synthesizes the long-term shipborne observations and a LES model
 490 to explore the phenomena of negative SAT-SST during advection fog over the NWP
 491 (referred to ssH fog). The UCLA-LES successfully simulates a fog event with ssH fog
 492 and captures the diurnal variation in SAT-SST during the fog episode. The simulation
 493 results highlight the strong influence of the LWC effect at the fog top on the formation
 494 of ssH fog.

495 Long-term shipborne observations reveal the prevalence of advection fog along
 496 the cold flank of the SST front in the NWP during the boreal summer. The ssH fog often
 497 occurs downstream of the regime of the advection fog with positive SAT-SST. The
 498 relative frequency ssH during episodes of advection fog is $\sim 27.5\%$ in JJA, which is
 499 roughly consistent with the results over the summertime Yellow Sea (Yang et al. 2021)
 500 and wintertime northeast Pacific (Li et al. 2022). Furthermore, our findings reveal, for
 501 the first time, that the relative frequency of ssH fog exhibits a distinct diurnal cycle,
 502 with a peak occurrence ($\sim 34.5\%$) before sunrise and a trough occurrence ($\sim 18.8\%$) in
 503 the afternoon (Fig. 2b). This suggests that the thermal dynamics and associated
 504 turbulence structure of advection fog exhibit significant diurnal variation.

505 From a Lagrangian perspective, we utilize the turbulence-closure UCLA-LES
 506 model to simulate an advection fog event over the NWP from 01 to 04 July 2013, which
 507 exhibits similar characteristics to the observations of this sea fog case and long-term

508 features of ssH fog. Surprisingly, the LES model successfully reproduces the diurnal
509 variation in SAT-SST of the observations when incorporating diurnal solar radiation,
510 indicating that the model captures the essential processes responsible for ssH fog.

511 We analyzed the LES simulation with constant solar radiation in detail, which also
512 produces ssH fog during the advection fog episode. Before the fog formation, the
513 decreased SST over the oceanic front cools the near-surface air through the mechanical
514 turbulence and triggers fog occurrence. Around the fog initiation, the cold sea surface
515 drives a stable layer below 40 m in altitude, which decouples the fog layer from the sea
516 surface. Once the surface vapor condenses, in the perspective of the fog layer, the fog-
517 top LWC effect rapidly exceeds the near-surface mechanical cooling within ~2 hours
518 after the fog formation (Fig. 9), when the air column is still on the SST front. A thermal
519 turbulence interface, separating the layers characterized by thermal and mechanical
520 turbulence, well depicts the evolution of the vertical turbulence structure (Fig. 10a).
521 The thermal turbulence from the fog top gradually develops downward to transport the
522 fog-top LWC effect and reaches the surface 43 hours after the fog formation, leading to
523 the SAT drops below SST. The occurrence time of ssH fog and minimum SAT-SST (-
524 0.65 K) is close to observation result (-1 K).

525 In the LES simulation with diurnal cycle radiation, the enhancement of LWC
526 during night causes the thermal turbulent interface to reach the surface, leading to the
527 occurrence of ssH fog. At daytime, the thermal turbulent interface moves away from
528 the surface and SAT rises above SST due to weakened LWC. This result is consistent
529 with the observed variations in SAT-SST, while the simulated SAT-SST is weaker than
530 observations. This suggests that the LWC is underestimated in the model, which could
531 be related to the model vertical resolution.

532 Previous studies have primarily focused on the diurnal variation of fog frequency
533 using observational data and models (O'Brien et al. 2013; Liu et al. 2021), but there has
534 been a lack of research on the diurnal variation of air-sea temperature difference. The
535 reason is that sea fog evolution are not as strongly influenced by the diurnal variation
536 of surface temperature as radiation fog on land (Koračin and Dorman 2017), there is
537 weak variability in SST during sea fog episodes. Kim and Yum (2013) the investigated

538 the effect of diurnal variation in radiation on advection fog formation by PAFOG model
539 but not discussed the diurnal variation in SAT-SST during fog due to the fog period is
540 short. This paper verifies, from both observational and modeling perspectives, that sea
541 fog exhibits significant diurnal variations in air-sea temperature difference, primarily
542 regulated by LWC at the fog top and thermal turbulence.

543 Our LES results suggest ssH fog formation is characterized by a thermal turbulent
544 layer, induced by the LWC at the fog top, that pervades the entire fog layer and cools
545 the near-surface air below the sea surface temperature (SST). Previous studies primarily
546 used on the near-surface liquid water in sea fog to validate the weather model
547 performance in simulating sea fog (e.g., Gao et al. 2007; Yang et al. 2018; 2019).
548 Considering the limited availability of observations on the vertical structure of fog over
549 the open sea, the observations of air-sea temperature differences during advection fog
550 events offers valuable insights for improving the modeling of the thermal turbulence
551 induced by the LWC at the fog top. The presence of ssH fog signals a pronounced LWC
552 at the fog top and thorough mixing of thermal turbulence within the layer. Consequently,
553 refining weather models to account for air-sea temperature differences enables more
554 precise sea fog simulations, especially in terms of the thermal turbulence within fog
555 layer. For instance, Yang et al. (2019) used top-down mixing parameterization in the
556 WRF model to characterize turbulence from the fog top. While the thermal turbulence
557 is explicitly resolved in UCLA-LES. Comparing these models' simulation results may
558 refine the turbulence parameterization in weather models, a desirable aim for future
559 research.

560 Yang et al. (2021) applied a weaker subsidence and did not simulate ssH fog. Our
561 simulation results demonstrate that descending motion plays an important role in
562 modulating the LWC at the fog top. Thus, stronger descending motion leads to longer
563 fog duration (72 h vs 55 h in Yang et al. 2021) and lower fog top height (380 m vs 580
564 m in Yang et al. 202). These findings indicate that large-scale descending motion
565 modulates the characteristics of fog by altering the fog-top LWC.

566

567 **Acknowledgments.** This work is supported by the National Key Research and

568 Development Program of China (2018YFA0605700), and the Natural Science
569 Foundation of China (41875012). L. Y. are supported by the National Key R&D
570 Program of China (2021YFB2601701), and S. D. are supported by Natural Science
571 Foundation of Shandong Province (ZR2019ZD12).

572

573 **Open Research**

574 **Data Availability Statement**

575 The data used in this study are obtained from the ECMWF which is available at
576 <https://www.ecmwf.int/en/forecasts/datasets/reanalysis-datasets/era5> and the ICOADS
577 data at <https://icoads.noaa.gov/>.

578

579

580 **Reference**

- 581 Bari, D., Bergot, T., & Khlifi, M. E. (2016). Local meteorological and large scale
582 weather characteristics of fog over the Grand Casablanca region, Morocco.
583 *Journal of Applied Meteorology and Climatology*, 55(8), 1731–1745.
584 <https://doi.org/10.1175/JAMC-D-15-0314.1>
- 585 Bergot, T. (2013). Small-scale structure of radiation fog: A large-eddy simulation study.
586 *Journal of the Royal Meteorological Society*, 139, 1099–1112.
- 587 Bergot, T. (2016). Large-eddy simulation study of the dissipation of radiation fog.
588 *Quarterly Journal of the Royal Meteorological Society*, 142, 1029–1040.
- 589 Bretherton, C. S., & Wyant, M. C. (1997). Moisture transport, lower-tropospheric
590 stability, and decoupling of cloud-topped boundary layers. *Journal of the*
591 *Atmospheric Sciences*, 54(1), 148–167. [https://doi.org/10.1175/1520-](https://doi.org/10.1175/1520-0469(1997)054%3C0148:MTL TSA%3E2.0.CO;2)
592 [0469\(1997\)054%3C0148:MTL TSA%3E2.0.CO;2](https://doi.org/10.1175/1520-0469(1997)054%3C0148:MTL TSA%3E2.0.CO;2)
- 593 Douglas, C. (1930). Cold fogs over the sea. *Meteorological Magazine*, 65, 133–135.
- 594 Caldwell, P., Bretherton, C. S., & Wood, R. (2005). Mixed-layer budget analysis of the
595 diurnal cycle of entrainment in southeast Pacific stratocumulus. *Journal of the*
596 *Atmospheric Sciences*, 62(10), 3775–3791.
- 597 Curry, J.A., & Herman, G. F., (1985). Infrared radiative properties of summertime
598 Arctic stratus clouds. *Journal of Climate Apply Meteorology*, 24, 525–538.
- 599 Draxler, R. R., & Rolph, G. D. (2010). HYSPLIT (HYbrid Single-Particle Lagrangian
600 Integrated Trajectory) model access via NOAA ARL READY website ([http://ready.](http://ready.arl.noaa.gov/HYSPLIT.php)
601 [arl.noaa.gov/HYSPLIT.php](http://ready.arl.noaa.gov/HYSPLIT.php)), NOAA Air Resources Laboratory. *Silver Spring*,
602 MD, 25(1).
- 603 Findlater, J., Roach, W., & McHugh, B. (1989). The haar of north-east Scotland.
604 *Quarterly Journal of the Royal Meteorological Society*, 115(487), 581–608.
- 605 Fu, Q., & Liou, K. N. (1993) Parameterization of the radiative properties of cirrus
606 clouds. *Journal of the Atmospheric Sciences*, 50, 2008–2025.
- 607 Fu, G., & Song, Y. J. (2014). Climatic characteristics of sea fog frequency over the
608 North Pacific Ocean. *Periodical of Ocean University of China*, 44(10), 35–41.

609 Gao, S., Lin, H., Shen, B., & Fu, G. (2007). A heavy sea fog event over the Yellow Sea
610 in March 2005: Analysis and numerical modeling. *Advances in Atmospheric*
611 *Sciences*, 24(1), 65–81. <https://doi.org/10.1007/s00376-007-0065-2>

612 Gerber, H., Malinowski, S. P., Brenguier, J. L., & Burnet, F. (2005). Holes and
613 entrainment in stratocumulus. *Journal of the Atmospheric Science*, 62, 443-459.

614 Gerber, H., Frick, G., Malinowski, S. P., Jonsson, H., Khelif, D., & Krueger, S. K.
615 (2013). Entrainment rates and microphysics in POST stratocumulus. *Journal of*
616 *Geophysical Research: Atmospheres*, 118, 1-16.

617 Gerber, H., Malinowski, S., Bucholtz, A. & Thorsen, T. (2014). Radiative Cooling of
618 Stratocumulus. Extended Abstract. 14 Atmospheric Radiation Conference,
619 American Meteorology Society, Boston, MA, 7-11 July, paper 9.3.

620 Guan, H., Yau, M. K., & Davies, R. (1997). The effects of longwave radiation in a small
621 cumulus cloud. *Journal of the Atmospheric Sciences*, 54(17), 2201–2214.
622 [https://doi.org/10.1175/1520-0469\(1997\)054%3C2201:TEOLRI%3E2.0.CO;2](https://doi.org/10.1175/1520-0469(1997)054%3C2201:TEOLRI%3E2.0.CO;2)

623 Gultepe, I., Tardif, R., Michaelides, S. C., Cermak, J., Bott, A., Bendix, J., et al. (2007).
624 Fog research: A review of past achievements and future perspectives. *Pure and*
625 *Applied Geophysics*, 164(6-7), 1121–1159. [https://doi.org/10.1007/s00024-007-](https://doi.org/10.1007/s00024-007-0211-x)
626 [0211-x](https://doi.org/10.1007/s00024-007-0211-x)

627 Hersbach, H., Bell, B., Berrisford, P., Hirahara, S., Horányi, A., Muñoz-Sabater, J., et
628 al. (2020). The ERA5 global reanalysis. *Quarterly Journal of the Royal*
629 *Meteorological Society*. <https://doi.org/10.1007>

630 Hu, R. J., Dong, K. H., & Zhou, F. X. (2006). Numerical experiments with the advection,
631 turbulence and radiation effect in the sea fog formation process (in Chinese).
632 *Advance in Marine Science*, 24(2), 156–165.

633 Huang, H., Liu, H., Huang, J., Mao, W., & Bi, X. (2015). Atmospheric boundary layer
634 structure and turbulence during sea fog on the southern China coast. *Monthly*
635 *Weather Review*, 143(5), 1907-1923.

636 Schwenkel, J., & Maronga, B. (2019). Large-eddy simulation of radiation fog with
637 comprehensive two-moment bulk microphysics: Impact of different aerosol
638 activation and condensation parameterizations. *Atmospheric Chemistry and*

639 *Physics*, 19, 7165–7181.

640 Lamb, H. (1943). Haars or North Sea fogs on the coasts of Great Britain. Meteorology
641 Office Publication M. O. 504, 24 pp.

642 Leipper, D. F. (1948). Fog development at San Diego, California. *Journal of Marine*
643 *Research*, 7, 337–346.

644 Leipper, D. F. (1994). Fog on the U. S. West Coast, a review. *Bulletin of the American*
645 *Meteorological Society*, 72, 229–240.

646 Lewis, J. M., Koraćin, D., & Redmond, K. T. (2004). Sea fog research in the United
647 Kingdom and United States: A historical essay including outlook. *Bulletin of the*
648 *American Meteorological Society*, 85(3), 395–408.

649 Lilly, D. K. (1967). The representation of small scale turbulence in numerical
650 simulation experiments. *IBM Scientific Computing Symposium on Environmental*
651 *Sciences*, Yorktown Heights, NY, International Business Machines, 195–210.

652 Li, X., Zhang, S., Koraćin, D., Yi, L., & Zhang, X. (2022). Atmospheric conditions
653 conducive to marine fog over the northeast Pacific in winters of 1979–2019.
654 *Frontiers in Earth Science*, 10, 942846.

655 Liu, J. W., Sun, Y., & Yang, L. (2021). Interannual variability in summertime sea fog
656 over the Northern Yellow Sea and its association with the local sea surface
657 temperature. *Journal of Geophysical Research: Atmospheres*, 126(15),
658 e2020JD034439.

659 Long, J., Zhang, S., Chen, Y., Liu, J., & Han, G. (2016). Impact of the Pacific-Japan
660 teleconnection pattern on July sea fog over the northwestern Pacific: Interannual
661 variations and global warming effect. *Advances in Atmospheric Sciences*, 33, 511–
662 521.

663 Jiang, H., Xue, H., Teller, A., Feingold, G., & Levin, Z. (2006). Aerosol effects on the
664 lifetime of shallow cumulus. *Geophysical Research Letters*, 33, L1486.

665 Kim, C. K., & Yum, S. S. (2013). A study on the transition mechanism of a stratus cloud
666 into a warm sea fog using a single column model PAFOG coupled with WRF.
667 *Asia-Pacific Journal of Atmospheric Sciences*, 49, 245-257.

668 Kunkel, B. A. (1984). Parameterization of droplet terminal velocity and extinction

669 coefficient in fog models. *Journal of Climate Applied Meteorology*, 23, 34–41,
670 [https://doi.org/10.1175/1520-0450\(1984\)023,0034:PODTVA.2.0.CO;2](https://doi.org/10.1175/1520-0450(1984)023<0034:PODTVA.2.0.CO;2).

671 Koračin, D., Leipper, D. F., & Lewis, J. M. (2005). Modeling sea fog on the U. S.
672 California coast during a hot spell event. *Geofizika*, 22(1), 59–82.

673 Koračin, D., Lewis, J., Thompson, W. T., Dorman, C. E., & Businger, J. A. (2001).
674 Transition of stratus into fog along the California coast: Observations and
675 modeling. *Journal of the Atmospheric Sciences*, 58(13), 1714–1731.
676 [https://doi.org/10.1175/1520-0469\(2001\)058%3C1714:TOSIFA%3E2.0.CO;2](https://doi.org/10.1175/1520-0469(2001)058%3C1714:TOSIFA%3E2.0.CO;2)

677 Koračin, D., & Dorman, C. E. (Eds.) (2017). *Marine fog: Challenges and advancements*
678 *in observations, modeling, and forecasting* (pp., 291–343). Zurich: Springer
679 International Publishing.

680 Maronga, B., & Reuder, J. (2017). On the formulation and universality of Monin-
681 Obukhov similarity functions for mean gradients and standard deviations in the
682 unstable surface layer: Results from surface-layer resolving large-eddy
683 simulations. *Journal of the Atmospheric Sciences*, 74, 989 – 1010.

684 McGibbon, J., & Bretherton, C. S. (2017). Skill of ship-following large-eddy
685 simulations in reproducing MAGIC observations across the northeast Pacific
686 stratocumulus to cumulus transition region. *Journal of Advances in Modeling*
687 *Earth Systems*, 9, 810–831.

688 Nakanishi, M. (2000). Large-eddy simulation of radiation fog. *Boundary-Layer*
689 *Meteorolog*, 94, 461–493.

690 O’Brien, T. A., Sloan, L. C., Chuang, P. Y., Faloona, I. C., & Johnstone, J. A. (2013).
691 Multidecadal simulation of coastal fog with a regional climate model. *Climate*
692 *Dynamics*, 40, 2801–2812.

693 Petterssen, S. (1938). On the causes and the forecasting of the California fog. *Bulletin*
694 *of the American Meteorological Society*, 19(2), 49–55.

695 Pincus, R., Baker, M. B., & Bretherton, C. S. (1997). What controls stratocumulus
696 radiative properties? Lagrangian observations of cloud evolution. *Journal of the*
697 *Atmospheric Sciences*, 54, 2215–2236.

698 Pincus, R., & Stevens, B. (2009). Monte Carlo spectral integration: A consistent

699 approximation for radiative transfer in large eddy simulations. *Journal of*
700 *Advances in Modeling Earth Systems*, 1, 9.

701 Rodhe, B. (1962). The effect of turbulence on fog formation. *Tellus*, 14, 49-86.

702 Rogers, D. P., & Koraćin, D. (1992). Radiative transfer and turbulence in the cloud-
703 topped marine atmospheric boundary layer. *Journal of the Atmospheric Sciences*,
704 49(16), 1473–1486.

705 Savic-Jovicic, V., & Stevens, B. (2008). The structure and mesoscale organization of
706 precipitating stratocumulus. *Journal of the Atmospheric Sciences*, 65, 1587–1605.

707 Seifert, A., & Beheng, K. D. (2001). A double-moment parameterization for simulating
708 auto conversion, accretion, and self-collection. *Atmospheric Research*, 59–60,
709 265–281.

710 Smagorinsky, J. S. (1963). General circulation experiments with the primitive equations.
711 Part I: The basic experiment. *Monthly Weather Review*, 91, 99–164.

712 Stevens, B. (2000). Cloud transition and decoupling in shear-free stratocumulus-topped
713 boundary layers. *Geophysical Research Letters*, 27, 2557–2560.

714 Stevens, B., Stevens, B., Lenschow, D. H., Faloona, I., Moeng, C. H., Lilly, D. K.,
715 Blomquist, B., Vali, G., Bandy, A., Campos, T., Gerber, H., Haimov, S., Morley,
716 B., & Thornton, D. (2003). On entrainment rates in nocturnal marine
717 stratocumulus. *Quarterly Journal of the Royal Meteorological Society*, 129, 3469–
718 3493.

719 Stevens, B., Moeng, C., Ackerman, A. S., Bretherton, C. S., Chlond, A., de Roode, S.,
720 Edwards, J., Golaz, J., Jiang, H., Khairoutdinov, M., Kirkpatrick, M. P., Lewellen,
721 D. C., Lock, A., Müller, F., Stevens, D. E., Whelan, E., & Zhu, P. (2005).
722 Evaluation of large-eddy simulations via observations of nocturnal marine
723 stratocumulus. *Monthly Weather Review*, 133, 1443–1462.

724 Stevens, B. (2010). Introduction to UCLA-LES: Version 3.2. 1. MPI Doc., 20 pp.

725 Taylor, G. I. (1917). The formation of fog and mist. *Quarterly Journal of Royal*
726 *Meteorological Society*, 43(183), 241–268. [https://doi.org/](https://doi.org/10.1002/qj.49704318302)
727 [10.1002/qj.49704318302](https://doi.org/10.1002/qj.49704318302)

728 Tokinaga, H., & Xie, S. P. (2009). Ocean tidal cooling effect on summer sea fog over

729 the Okhotsk Sea. *Journal of Geophysical Research: Atmospheres*, 114, D14102.

730 Trémant, M. (1987). La prévision du brouillard en mer. *Météorologie Maritime et*
731 *Activities. Oceanographiques Connexes Raport*, WMO, 20, 127.

732 Wang, B. H. (1985). *Sea fog* (p., 2). Beijing: China Ocean Press.

733 Wainwright, C., & Richter, D. (2021). Investigating the sensitivity of marine fog to
734 physical and microphysical processes using large-eddy simulation. *Boundary-*
735 *Layer Meteorology*, 181, 473-498.

736 Wyant, M. C., Bretherton, C. S., Rand, H. A., & Stevens, D. E. (1997). Numerical
737 simulations and a conceptual model of the stratocumulus to trade cumulus
738 transition. *Journal of the Atmospheric Sciences*, 54, 168–192.

739 Yamaguchi, T., & Randall, D. A. (2008). Large-eddy simulation of evaporatively driven
740 entrainment in cloud-topped mixed layers. *Journal of the Atmospheric Sciences*,
741 65(5), 1481–1504.

742 Yang, Y., Hu, X. M., Gao, S., & Wang, Y. (2018). Sensitivity of WRF simulations with
743 the YSU PBL scheme to the lowest model level height for a sea fog event over the
744 Yellow Sea. *Atmospheric Research*, 215, 253–267.

745 Yang, Y., & Gao, S. (2019). The impact of turbulent diffusion driven by fog-top cooling
746 on sea fog development. *Journal of Geophysical Research: Atmospheres*, 125,
747 e2019JD031562. <https://doi.org/10.1029/2019JD031562>

748 Yang, L., Liu, J. W., Ren, Z. P., Xie, S. P., Zhang, S. P., & Gao, S. H. (2018).
749 Atmospheric conditions for advection-radiation fog over the Western Yellow Sea.
750 *Journal of Geophysical Research: Atmospheres*, 123, 5455–5468.
751 <https://doi.org/10.1029/2017JD028088>

752 Yang, L., Liu, J. W., Xie, S. P., & Shen, S. S. (2021). Transition from fog to stratus over
753 the northwest Pacific Ocean: Large-eddy simulation. *Monthly Weather Review*,
754 149, 2913-1925.

755 Zhang, S. P., & Ren, Z. P. (2010). The influence of thermal effects of underlying
756 surface on the spring sea fog over the Yellow Sea—Observations and numerical
757 simulation (in Chinese). *Acta Meteorologica Sinica*, 68, 116–125.

758 Zhang, S. P., Li, M., Meng, X. G., Fu, G., Ren, Z. P., & Gao, S. H. (2012). A comparison
759 study between spring and summer fogs in the Yellow Sea—Observations and
760 mechanisms. *Pure and Applied Geophysics*, 169(5-6), 1001–1017.
761 <https://doi.org/10.1007/s00024-011-0358-3>
762 Zhang, S., Chen, Y., Long, J., & Han G. (2014). Interannual variability of sea fog
763 frequency in the Northwestern Pacific in July. *Atmospheric Research*, 151, 189–
764 199.
765